Mechanics of normal fault networks subject to slip-weakening friction

Sylvie Wolf, Isabelle Manighetti, Michel Campillo, I. R. Ionescu

Geophys. J. Int. (2006) **165,** 677–691 doi: 10.1111/j.1365-246X.2006.02910.x

Mechanics of normal fault networks subject to slip-weakening friction

S. Wolf,[1,2] I. Manighetti,[1] M. Campillo[1] and I. R. Ionescu[2]

[1]*Laboratoire de Géophysique Interne et Tectonophysique, Université Joseph Fourier et CNRS, BP* 53X, 38041 *Grenoble Cedex* 9, *France. E-mail: sylvie.wolf@free.fr*

[2]*Laboratoire de Mathématiques, Université de Savoie et CNRS, Campus Scientifique,* 73376 *Le Bourget-du-Lac Cedex, France*

Accepted 2006 January 11. Received 2005 August 3; in original form 2004 February 10

SUMMARY

We seek to understand how the stress interactions and the slip-weakening process combine within a non-coplanar, normal fault network to allow a slip instability to develop, and shape the final slip distribution on the system. In a first part, we perform a non-linear spectral analysis to investigate the conditions of stability and the process of slip initiation in an antiplane non-coplanar fault system subject to a slip-dependent friction law. That numerical model allows determining the zones that are able to slip within a fault network, as well as the location of the stress singularities. The resulting slip profiles on the faults show only a few different shapes, some of them with long, linear sections. This leads to formulate a general classification of slip profiles that can be used to infer the degree of fault interaction within any non-coplanar system. In a second part of work, we use our modelling to try reproducing the cumulative slip profiles measured on three real normal interacting faults forming a large-scale *en echelon* system. For that, we assume that cumulative slip profiles can be compared to the first static modal solution of our conceptual model. We succeed reproducing the profiles quite well using a variable weakening along the faults. Overall, the weakening rate decreases in the direction of propagation of the fault system. Yet, modelling the slip along the propagating, isolated termination segment of the system requires an unlikely distribution of weakening. This suggests that factors not considered in our analysis may contribute to slip profile shaping on isolated, propagating faults.

Key words: earthquakes, fault interaction, fault slip, normal faulting, spectral analysis, stress distribution.

1 INTRODUCTION

Although most mechanical and seismological models consider faults and fault systems as planar and/or coplanar structures (i.e. faults lying in the same plane), real faults and systems rarely are that simple. At all scales, faults are segmented, and geologists have shown for long that such segments rarely are coplanar along the fault to which they belong. As a matter of fact, the *en echelon* arrangement of segments along faults is one of the most common fault geometry observed worldwide. Faults also rarely are isolated, but instead develop as systems where secondary, smaller faults form off a main fault plane and connect it. A classical example is that of 'horsetail terminations' and branching secondary faults that are observed to form at many scales at the ends and along strike-slip faults. It results that the mechanics of non-coplanar fault networks is a key issue in the understanding of earthquakes and faulting. Among other questions, one is to understand how faults interact within a non-coplanar system, and how such interactions may govern and shape the slip distribution within the system. We address these questions in the present study. More specifically, we seek to characterize the 'stress interactions' that occur within a non-coplanar fault system once this system has just started to slip. Our approach is thus dynamic. In coplanar fault systems, the question of stress interaction is quite simple: any slip occurring at one place of the system loads the rest of its plane, so that anywhere the fault system experiences a stress increase before it possibly slips. In non-coplanar fault systems, the problem is more complex: slip occurring at one spot of the system can either load or unload the other parts of the system, depending on their position from the slip 'spot'. In other words, some portions of a non-coplanar fault system may experience a stress increase while some others may experience a stress decrease (stress shadow). From a dynamic point of view, this means that some portions of a non-coplanar fault system will slip as a response to slip occurring elsewhere on the system, while some others will not. It is, therefore, critical to characterize the 'stress interactions' that occur within a non-coplanar system that has just started to slip, for this may help anticipating which parts of the system will eventually slip and what the resulting slip function will be.

We consider a non-coplanar fault system with a simple geometry, and assume that that system is subject to slip-weakening friction. As slip on a fault is required by the friction laws to occur in the direction and sense of traction (i.e. no back-slip allowed), consistent slip solutions can only be found from non-linear analyses. We, therefore, develop and perform one of such non-linear analyses, to seek predicting the final slip function on our 'active' fault system. The novelty of the present work is that it allows examining together the effects of dynamic stress transfer and of weakening on the slip distribution. Besides, contrary to the few previous studies (see below) that have been carried out on dynamic fault interaction, our model allows examining the slip distribution that results from the long-term evolution of the fault system. More precisely, our model allows, as a first step, to characterize the combined effects of stress interaction and weakening on the final slip distribution. The numerical method can then be used to tentatively reproduce real (known) slip profiles on geological faults having a given (known) geometry (see details below). The comparison between the results from our conceptual model and the actual observations points out two critical issues: can the 'best-fitting' slip-weakening functions inferred on the faults be considered as 'realistic' and what are the mechanical factors that should be introduced in the model in addition to stress transfer and friction, to make it able to fully reproduce the observed slip profiles?

As said before, many studies have already been carried out on stress interactions within non-coplanar fault systems. These previous works have either focused on the study of cumulative long-term slip profiles, or on that of coseismic slip. However, works on cumulative slip profiles generally have only addressed the static solution of the problem and have ignored the possibility of progressive weakening. On the other hand, works on coseismic slip have concentrated on dynamic rupture propagation, using specific numerical modelling that cannot be used to examine the longer-term evolution of slip.

Below we briefly review these works, focusing on the methodologies used to model fault interaction.

Okada (1992), following Comninou & Dunders (1975), calculated the static stress changes due to an earthquake fault slip, and inferred the stress overload on adjacent faults, in the presence of a free surface. However, these calculations are linear, so that fault interaction is simplistically modelled as the superposition of the static stress fields produced by each fault in the system. Although this cannot fully represent the real processes, these computations have since then been extensively used, with more or less success, in particular to predict the possible increase of seismic activity on faults adjacent to an earthquake rupture (e.g. King *et al.* 1994). More recently, a refined version of the model has been proposed (Fitzenz & Miller 2001) that also includes pre-stresses and fluid pressure; this shows that increased pore pressure (poroelastic effects) favours stress transfer and triggering of earthquakes from one fault to the other.

Considering faults as cracks in an elastic medium under compressive stresses (i.e. stress on cracks does not exceed the Coulomb limiting stress), Segall & Pollard (1980) computed the static state of stress around interacting non-coplanar faults and deduced the geometry of the possible resulting secondary fracturing. The model was subsequently extended by several authors (e.g. Bürgmann *et al.* 1994; Willemse 1997; Crider & Pollard 1998). Baud & Reuschlé (1997) quantified the effect of interaction on the crack propagation path, and showed that interaction commonly favours branching and coalescence of faults within the system they belong to. Detailed methods of resolution of such problems (in particular theoretical determination of the stress intensity factors of interacting cracks) can be found in Pucik (1972) and Ishida (1973). Finally, Umeda *et al.* (1996) suggested that crack interaction can be responsible for rupture nucleation and/or arrest depending on the constructive or destructive 'interferences' (loading or unloading) made by cracks. Yet, although useful, crack models cannot be retained as fully satisfactory as they ignore the possibility of progressive weakening.

Other models, which are neither dislocation nor crack models (i.e. neither the displacement nor the stress drop distributions are prescribed), have also been proposed to deal with fault interaction. For instance, using a discrete quasi-static model which simulates successive ruptures on two overlapping faults, Robinson & Benites (1995) showed that fault interaction plays a part in the organization of seismicity on the fault system. Spyropoulos *et al.* (2002) studied crack growth and coalescence in a spring block analogue allowing some friction to be taken into account. They found scaling laws for crack slip and length, and pointed out the lack of symmetry of the resulting slip profiles. Depending on the rate of strain imposed at the boundaries of the system, faults grow isolated (with no or little interaction) or coalesce to others (strong interaction). These two behaviours lead to different distributions of fault sizes. Finally, Harris & Day (1993) addressed the dynamic, that is, coseismic part of the problem : they studied numerically the jump of a propagating rupture from a segment to another using a slip-weakening friction on the fault planes. More recently, Aochi & Madariaga (2003) simulated the propagation of the 1999 Izmit earthquake rupture and showed how the dynamic interaction between the major non-coplanar segments conditioned the rupture propagation.

All the models above have clearly pointed out the importance of stress interactions in non-planar slip processes (i.e. slip on non-coplanar faults), whether these are seismic (i.e. resulting from one earthquake) or cumulative (i.e. resulting from several earthquakes and/or creep). However, as said before, very few of them have investigated the coupling between these stress interactions and the constitutive friction laws on the faults, especially the weakening process, and, to our knowledge, none of them have attempted to compare numerical results with real long-term slip distributions. We address this issue here.

We pose the problem in its simplest form : we consider the behaviour of a 2-D antiplane fault network (i.e. normal faults) subject to a basic slip-weakening friction law. During earthquakes, the weakening process is the one responsible for fault instability resulting in earthquake initiation followed by rupture propagation and slip. We define the earthquake initiation phase as the period of time extending between the first perturbation of the mechanical conditions on the fault system, and the onset of rupture propagation associated with wave radiation. Such a nucleation process has been observed in laboratory experiments (e.g. Ohnaka *et al.* 1987; Ohnaka & Kuwahara 1990). The friction on the experimental nucleating faults could be satisfactorily described by a slip-weakening law (e.g. Ohnaka *et al.* 1987).

Taking these experimental results as a basis, Dascalu *et al.* (2000) studied the antiplane shearing of a finite fault, and performed a spectral analysis to relate fault stability and slip weakening, using an integral equation method. This led them to introduce a universal non-dimensional constant β_0^* that appeared to only depend on the fault geometry. They showed that this constant alone allows discriminating the stable (i.e. slipping at the velocity imposed as an external condition) and unstable (i.e. accelerating rapidly toward a seismic event) fault states. Non-uniform stress loading on planar faults was then studied by Uenishi & Rice (2002), basically with the same modal approach than that of Dascalu *et al.* (2000). These authors reached the same conclusions regarding the value and

interpretation of β_0^*. Then Campillo *et al.* (2001) used an argument of spectral equivalence as a renormalization technique to investigate the case of a fault with heterogeneous strength. Finally, Voisin *et al.* (2002) used a finite element method to study the case of several coplanar fault segments. By computing the evolution of their stability limit β_0 while these segments interact, Voisin *et al.* showed that coplanar interaction increases fault instability, a property later confirmed by the stability analysis of a periodic distribution of segments (Campillo *et al.* 2004). In all these works, the eigenfunction associated to β_0 is shown to hold the characteristic pattern of the displacement field on the modelled faults when those are in a meta-stable position of equilibrium (i.e. close to their limit of stability, hence infinitely slowly slipping) and subject to mechanical weakening. In other words, this kind of analysis can be used to describe the slip distribution as it would be on a fault system subject to slow sliding. The slip profiles deduced from the conceptual model can thus reasonably be compared to long-term slip profiles on real faults.

We follow these last works to investigate the stability limit of non-coplanar faults having different geometries. While the stability of a system made of coplanar faults simply increases with the distance between the faults, the stability of a non-coplanar system varies in a much more complex way, due to the effect of local stress shadows. Using the same modal approach than the one described above, we deduce meta-stable slip distributions on faults belonging to systems of various geometries. We find that most slip profiles exhibit long, quasi-linear sections, hence do not resemble the classical elliptical slip distributions expected for isolated faults in an elastic medium.

We then face our numerical results to a real example of non-coplanar fault system, made of three, 20–30 km-long, *en echelon*, active normal faults. We chose that system in Afar (East Africa) because faults there are active, while the boundary conditions and long-to short-term evolution of faulting are well known (e.g. Tapponnier *et al.* 1990; Manighetti *et al.* 1998, 2001a,b). Besides, the Afar faults are among the rare to have their cumulative slip profiles precisely measured (Manighetti *et al.* 2001a). This gives us the opportunity to face some of these real slip profiles to the meta-stable solutions of our modelling. That comparison allows us to infer possible slip-weakening variations along the three example faults, while estimating the state of stress on their planes and at their tips. While our modelling is 'too simple' to be able to reproduce the details or chronology of the fault system growth (more parameters should be taken into account, such as damage around fault terminations, pre-stresses, etc., e.g. Scholz 2002; Manighetti *et al.* 2004), its comparison to real data allows highlighting some of the major 'ingredients' that contribute to the process of fault growth: stress shadowing, along-strike variation of slip weakening, existence of barriers, necessity of considering off-fault damage.

2 THE TIME-DEPENDENT PROBLEM

We consider the 2-D antiplane shearing of two parallel finite fault segments in an unbounded homogeneous linear elastic space (see Fig. 1). Systems of three or more segments will be investigated later. We denote by Γ_f the potential geometrical support of the fault system, but the effective fault segments, that is, the effective slipping zones, which depend on fault interaction, will be determined by the calculations.

Let a be a characteristic length; when several fault segments of same length are considered, a will be their common half-length. In the following, x and y are non-dimensional coordinates rescaled by

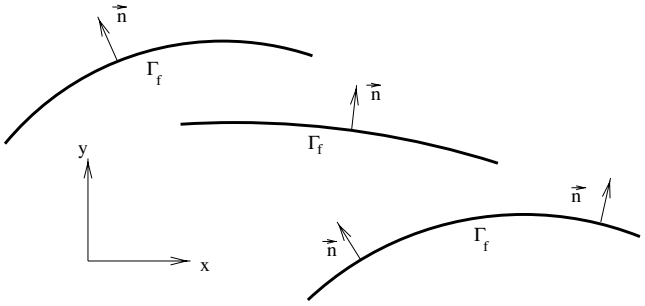

Figure 1. Antiplane normal fault definition. Fault segments lie in the xy plane. Their geometrical support is the segmented curve Γ_f. The local normal of Γ_f in the xy plane is denoted by n. Displacement $u \equiv u_z$ and shear stresses σ_{zx} and σ_{zy} are perpendicular to the xy plane.

a. The contact on the fault is described by a slip-dependent friction law. We assume an antiplane configuration, that is, the displacement field $u \equiv u_z$ is perpendicular to the faults, and does not depend on z. The displacement is, therefore, denoted simply by $u(t, x, y)$, t being the time variable. The characteristic parameters of the elastic medium are the shear modulus G, the density ρ and the shear velocity $c = \sqrt{G/\rho}$. The non-vanishing shear stress components are $\sigma_{zx}(t, x, y) = \sigma_{zx}^{\infty}(x, y) + \frac{G}{a}\partial_x u(t, x, y)$ and $\sigma_{zy}(t, x, y) = \sigma_{zy}^{\infty}(x, y) + \frac{G}{a}\partial_y u(t, x, y)$, where σ_{zx}^{∞} and σ_{zy}^{∞} are pre-stress components. On the fault support, that is, for $(x, y) \in \Gamma_f$, we denote by $\sigma_{nn}(x, y)$ the normal stress, and by $\sigma_{zn}^{\infty}(x, y)$ the shear pre-stress. The equation of motion is the scalar wave equation:

$$\partial_{t^2}^2 u(t, x, y) = \frac{c^2}{a^2}\nabla^2 u(t, x, y), \tag{1}$$

which holds for $t > 0$ and (x, y) outside Γ_f.

For $t > 0$ and $(x, y) \in \Gamma_f$, let us denote by $[w(t, x, y)]$ the jump of any variable w across Γ_f according to its local normal n.

The boundary conditions on Γ_f follow a slip-dependent friction law, with the additional constraint that the shear stress (including the pre-stress) cannot reverse on faults, so that the slip $[u]$ and slip rate $[\partial_t u]$ are non-negative. This assumption is common at small timescales in earthquake dynamics modelling, but is also admitted at reasonably large tectonic timescales when plates are moving at quasi-constant rates. This statement will be the cause of strong non-linearities in the modelling. Therefore, we formulate the constitutive law on the fault by :

$$[\partial_t u(t, x, y)] \geq 0, \tag{2}$$

$$[\sigma_{zn}(t, x, y)] = 0, \tag{3}$$

$$\sigma_{zn}(t, x, y) = -\mu([u(t, x, y)])\,\sigma_{nn}(x, y) \quad \text{if } [\partial_t u(t, x, y)] > 0, \tag{4}$$

$$\sigma_{zn}(t, x, y) \leq -\mu([u(t, x, y)])\,\sigma_{nn}(x, y) \quad \text{if } [\partial_t u(t, x, y)] = 0, \tag{5}$$

for all $(x, y) \in \Gamma_f$ and $t > 0$, where σ_{zn} is the shear stress acting on Γ_f and μ ($[u]$) is the friction coefficient.

The initial conditions are denoted by u_0 and u_1, that is,

$$u(0, x, y) = u_0(x, y), \quad \partial_t u(0, x, y) = u_1(x, y). \tag{6}$$

3 NON-LINEAR SPECTRAL ANALYSIS

In this subsection, we define the non-linear problem associated to the time-dependent problem stated above. To do this, we have to

assume a few simplifications. First, since our intention is to study the evolution of the system near an unstable equilibrium position, we shall suppose that, at each fault point, $\sigma_{zn}^{\infty} = -\sigma_{nn}\,\mu_s$, where $\mu_s = \mu(0)$ is the static value of the friction coefficient. This is not a very restrictive assumption, since, to equilibrate the system, some of the points of Γ_f will be spontaneously unloaded by stress interaction and locked. We remark that taking u as a constant satisfies eqs (1)–(5); hence $u \equiv 0$ is a meta-stable equilibrium position, and (u_0, u_1) may be considered as a small perturbation of this equilibrium.

As a second assumption, we shall suppose that the friction law is piecewise linear :

$$\begin{aligned}\mu([u]) &\le \mu_s \quad \text{if} \quad [u] = 0\\ &= \mu_s - \frac{\mu_s - \mu_d}{2L_c}[u] \quad \text{if} \quad 0 < [u] \le 2L_c\\ &= \mu_d \quad \text{if} \quad [u] > 2L_c,\end{aligned}$$

where μ_s and μ_d are the static and dynamic friction coefficients ($\mu_s > \mu_d$), and L_c is the critical half-slip. We can hereafter define the weakening rate α, which can be heterogeneous :

$$\alpha(x, y) = \frac{-\sigma_{nn}(x, y)(\mu_s(x, y) - \mu_d(x, y))}{GL_c(x, y)}.$$

Since we consider a *small* initial perturbation (u_0, u_1) of the equilibrium state $u \equiv 0$, we have a progressive slip growth such that $[u(t, x, y)] \le 2L_c(x, y)$ for $t \in [0, T_c]$ along the faults, where T_c is the critical time at which the slip on the fault reaches the critical value $2L_c$ at least at one point. Hence, for a first period $[0, T_c]$, called the initiation period, the boundary value problem on Γ_f is reduced to the following equations:

$$[u(t, x, y)] \ge 0 \text{ and } [\partial_n u(t, x, y)] = 0 \text{ for } (x, y) \in \Gamma_f, \tag{7}$$

$$\partial_n u(t, x, y) = -a\alpha(x, y)[u(t, x, y)] \text{ if } [u(t, x, y)] > 0, \tag{8}$$

$$\partial_n u(t, x, y) \le 0 \text{ if } [u(t, x, y)] = 0, \tag{9}$$

where ∂_n is the normal derivative.

We can now define the non-linear eigenvalue problem connected to eqs (1), (6) and (7)–(9):

Find $\Phi : \mathbb{R} \times \mathbb{R} \to \mathbb{R}$ and $\lambda^2 \in \mathbb{R}$ such that $\int_{-\infty}^{+\infty}\int_{-\infty}^{+\infty} \Phi^2(x, y)\,dx\,dy = 1$ and

$$\nabla^2\Phi(x, y) = \lambda^2\Phi(x, y), \tag{10a}$$

$$[\partial_n\Phi(x, y)] = 0 \text{ on } \Gamma_f, \tag{10b}$$

$$[\Phi(x, y)] \ge 0 \text{ and } \partial_n\Phi(x, y) \le 0 \text{ on } \Gamma_f, \tag{10c}$$

$$\partial_n\Phi(x, y) = -a\alpha(x, y)[\Phi(x, y)] \text{ or } [\Phi(x, y)] = 0 \text{ on } \Gamma_f. \tag{10d}$$

The main novelty of our modelling is that it can handle locked zones : Γ_f is the potential geometrical support of the fault system, but the effective slipping zone, included in Γ_f, is not given *a priori* but instead determined as a result of the calculations, hence as a function of stress interaction. A linear analysis would be sufficient if we would remove the locked part of Γ_f in the modelling. The non-linearity of our problem comes from the fact that the geometry of the slipping zone is one of the unknowns. The stress interactions produce large locked zones, so that the resulting slip profiles are different from what they would have been deduced from a linear analysis ignoring stress shadowing.

Let us examine in details the linear and non-linear eigenfunctions for a particular system of two overlapping parallel segments (see the geometry on Fig. 2). The first linear mode, plotted on Fig. 2 (left), has the smallest eigenvalue ($\beta_0^{\text{lin}} = 0.97$), but it cannot be retained because one of the segments is sliding backwards. The second linear mode (Fig. 2, middle) has a positive slip and a slightly larger eigenvalue ($\beta_1^{\text{lin}} = 1.17$). This mode is physically admissible (in that the slip is everywhere non-negative), but the first non-linear mode (Fig. 2, right)- admissible by construction - has a smaller eigenvalue ($\beta_0^{\text{nlin}} = 1.06$). We recall here the physical meaning of the eigenvalue : if the weakening rate exceeds this value, the corresponding eigenmode is triggered and grows exponentially. Hence, the first non-linear mode will be triggered before any linear (and admissible) one. It is worth noticing that the solution is not unique, for simple symmetry reasons: the dominant fault segment could have been the inhibited one, and vice versa.

Where fault segments do not or hardly overlap, the solutions of the linear system (10a), (10b), (10d) fulfil the inequality (10c) and the general solution of (1), (6), (7)–(9) can be decomposed on the infinite family of eigenfunctions of (10a), (10b), (10d) (see Dascalu *et al.* 2000; Voisin *et al.* 2002, for coplanar segments). By contrast, within non-coplanar fault systems where segments significantly overlap, the linear analysis leads to solutions that do not fulfil the condition of positivity on the slip. Therefore, a whole non-linear analysis must be carried out, and the decomposition above is no longer valid. However, one important result still holds: if we find an eigenfunction Φ with a positive eigenvalue $\lambda^2 \ge 0$, then $u(t, x, y) = e^{c|\lambda|t/a}\Phi(x, y)$ is a solution of (1), (6), (7)–(9) and $u \equiv 0$ is an unstable configuration.

In order to find the critical physical properties of the problem (directly related to α), which correspond to the loss of stability, we will focus on the case $\lambda^2 = 0$. In this case, the unknown is the weakening rate, but there is an infinite number of heterogeneous solutions $\alpha(x, y)$. Therefore, we denote by $\eta(x, y)$ the dimensionless function which defines the shape of $\alpha(x, y)$ along Γ_f. We assume that $a\alpha(x, y) = \beta\eta(x, y)$, and the unknown is the non-dimensional scaling factor β. The above eigenproblem becomes:

Find $\varphi : \mathbb{R} \times \mathbb{R} \to \mathbb{R}$ and $\beta > 0$ such that $\int_{-\infty}^{+\infty}\int_{-\infty}^{+\infty} \varphi^2(x, y)\,dx\,dy = 1$ and

Geometry

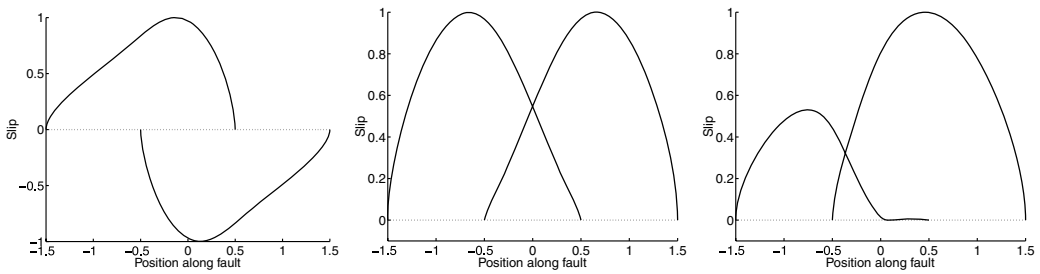

Figure 2. Left: the first linear eigenfunction. Middle: the second linear eigenfunction. Right: the first non-linear eigenfunction.

$$\nabla^2\varphi(x, y) = 0, \tag{11a}$$

$$[\partial_n\varphi(x, y)] = 0 \text{ on } \Gamma_f, \tag{11b}$$

$$[\varphi(x, y)] \geq 0 \text{ and } \partial_n\varphi(x, y) \leq 0 \text{ on } \Gamma_f, \tag{11c}$$

$$\partial_n\varphi(x, y) = -\beta\eta(x, y)[\varphi(x, y)] \text{ or } [\varphi(x, y)] = 0 \text{ on } \Gamma_f. \tag{11d}$$

To discriminate the stable and unstable behaviours, we need to compute β_0, which is the smallest eigenvalue of (11a)–(11d). Indeed, if $\beta > \beta_0$, then the eigenproblem (10a)–(10d) has a positive eigenvalue λ^2, that is, $u \equiv 0$ is an unstable solution of the non-linear problem.

$$\text{If} \quad \beta > \beta_0, \quad \text{then} \quad u \equiv 0 \quad \text{is unstable.} \tag{12}$$

Hence, assuming that the shape $\eta(x, y)$ of the weakening variations along the fault is known, the stability analysis of (1), (7)–(9) reduces to the computation of β_0. The associated eigenfunction describes the pattern to which the system is infinitely slowly evolving.

4 NUMERICAL RESOLUTION OF THE NON-LINEAR SPECTRAL PROBLEM

In this subsection, we briefly describe the finite element numerical method used to solve the non-linear spectral problem, which is detailed by Ionescu & Wolf (2005). Later, we will present the computation of the time-dependent problem to test the spectral method. The method for the time-dependent problem is not described in this paper, but rather in Badea *et al.* (2004).

Let us state the variational formulation of the problem (10a)–(10d), with $\Omega = \mathbb{R}^2 \backslash \Gamma_f$:

Find $\Phi : \mathbb{R} \times \mathbb{R} \to \mathbb{R}$ and $\lambda^2 \in \mathbb{R}$ such that

$$\int_\Omega \nabla\Phi(x, y) \cdot \nabla v(x, y)\, dx\, dy - \beta \int_{\Gamma_f} [\Phi(x, y)][v(x, y)]\, dx \geq -\lambda^2 \int_\Omega \Phi(x, y) v(x, y)\, dx\, dy, \tag{13}$$

for all test functions v such that $[v] \geq 0$ on Γ_f.

The variational formulation of (11a)–(11d) is deduced from (13) by setting $\lambda^2 = 0$. In both cases, the problem reduces to the computation of the smallest eigenvalue of a non-linear operator. This can be done by considering the successive iterates of the non-linear operator, after choosing an initial guess. The detailed algorithm can be found in Ionescu & Wolf (2005). We only discuss here the properties of our spatial discretization.

The classical P1 finite element method consists in covering Ω with a set of triangles and then approaching Φ by a function which is continuous and affine over each triangle. The domain Ω is unbounded, therefore, it is divided in two parts. The first one is a square that contains Γ_f and which boundary is *far enough* from the fault system. It is possible to cover exactly this square with triangles. The second part is infinite and can be covered with *infinite elements* (Beer & Meek 1981). The size of the elements in the square is automatically decreased in the regions where strong variations of the gradient are expected, using a *remeshing* strategy, based on the computation of the local error (Zienkiewicz & Zhu 1987). The implementation of these two techniques in our model are described in Ionescu & Wolf (2005).

5 RESULTS FOR TWO PARALLEL HOMOGENEOUS IDENTICAL STRAIGHT SEGMENTS

Our numerical model can be applied to any antiplane fault geometry. However, we start by the simplest case of two parallel, homogeneous (i.e. with same homogeneous weakening rate and initially at the static threshold), identical faults oriented along x (Fig. 3). The faults have a common half-length a. Their normal n lies along y. As shown in Fig. 3, the geometry of the two-faults system is completely determined by two parameters d and e, which define the separation distance between the two faults and their along-strike offset (hence overlap), respectively. Length g is an output of the calculations: it is the half-length of the effective slipping zone on the lower segment, and can be any value between 0 and a.

To illustrate stability, let us first present the results of two dynamical experiments with $a = 1$, $d = 0.5$, $e = 0.1$. The evolution of the velocity field is presented on Fig. 9 of Ionescu & Wolf (2005) for two homogeneous weakening rates $\alpha = 1.0$ and $\alpha = 1.2$. At $t = 0s$, each point on the faults is at the static threshold, and a small Gaussian velocity perturbation is applied at an arbitrary point. First, the shear waves propagate in a similar way in both cases, but slip grows faster for $\alpha = 1.2$. Then the behaviour changes depending on alpha. The slip on the faults with lower weakening rate ($\alpha = 1.0$) is rapidly stabilized so that the faults stop slipping. By contrast, the initiation phase does begin for the faults with faster weakening rate ($\alpha = 1.2$); the slip rate has a constant shape, with a locked zone on the lower fault, and it grows exponentially (see Badea *et al.* 2004, for details on the slip growth). Note that having each point originally at the threshold of failure does not force the system to slide globally. Instead, in both cases the lower fault is unloaded and thus locked by the upper one.

From result (12), and since $a = 1$ and $\eta(x, y) = 1$, we expect $1.0 < \beta_0 < 1.2$. The non-linear spectral computation gives $\beta_0 \simeq 1.06$. Hence, the physical meaning of the first eigenvalue is validated. This confirms that β_0 is a critical value of the friction parameter

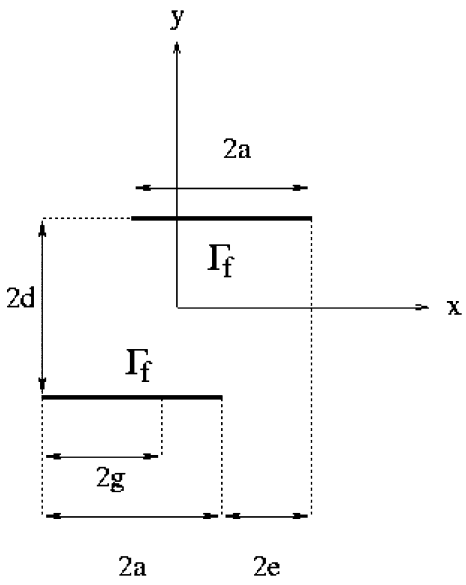

Figure 3. Fault geometry: two parallel segments of same half-length a. The input parameters are the half-separation d and the half-offset e. The half-length g of the effective slipping zone on the lower segment is an output of the calculations. In what follows, the top and bottom segments are called 'upper' and 'lower' faults, respectively.

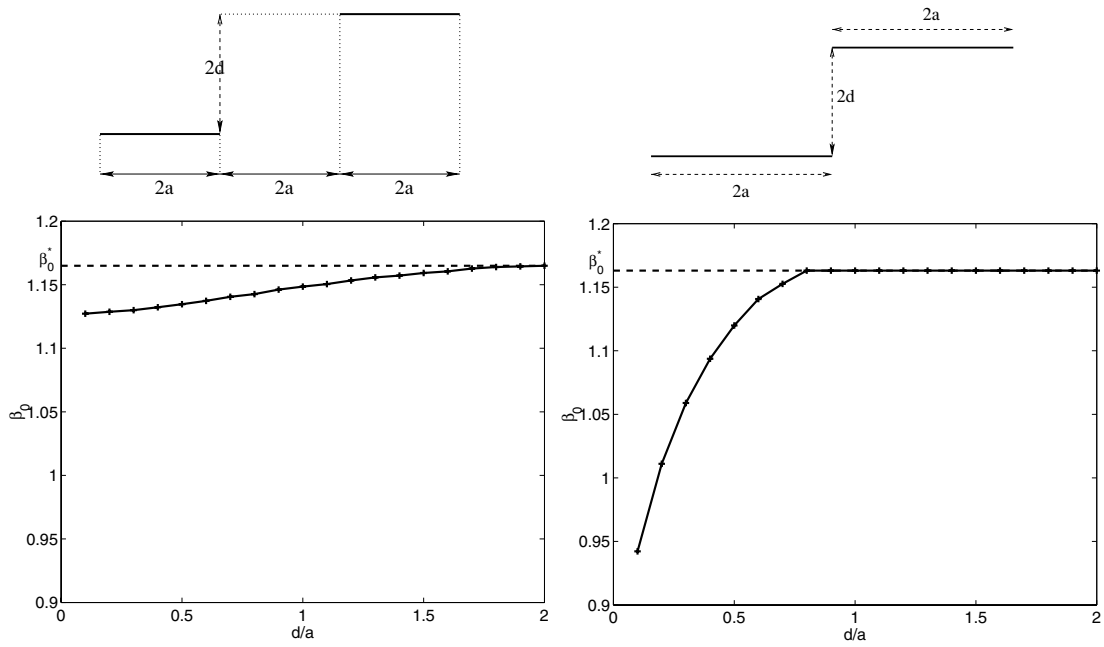

Figure 4. The first eigenvalue β_0 as a function of the distance d/a between the faults, for $e = 2a$ (**left**) and $e = a$ (**right**).

that governs the stability of the system. In addition, in the time-dependent experiment above, in the case where slip initiates, the half-length of the slipping zone ($g \simeq 0.78$) is determined early and found to be independent of the location of the initial perturbation. Therefore, it seems to be reasonable to approach the slip pattern by some eigenmode having a slipping zone, which is part of the unknowns. This argument justifies the non-linear spectral analysis.

To investigate the relationship between fault system stability and geometry, we look for the meta-stable modes, which correspond to β_0. We first study the case of two identical fault segments, that is, with same length and weakening rate that do not overlap. We examine the particular cases where $e = 2a$ and $e = a$ (see Fig. 3). The first eigenvalue β_0 is computed for a set of values of the separation distance d. In both cases, the two faults do not sustain any shadow effect, so that both are sliding globally ($g = a$). As one can see in Fig. 4, β_0 increases with the distance d separating the faults, up to β_0^*. However, β_0 is high and increases weakly with d in the case $e = 2a$. This means that the two faults hardly interact. By contrast, the variations of β_0 are great for the case $e = a$, and the critical value β_0^* is reached sooner (due to the shape of the region of positive shear stress generated by each fault). Once this value is reached, the faults stop interacting and both segments start consequently sliding independently (the linear analysis holds, and the first linear eigenvalue is double).

We now examine how the stability of the two-faults system varies as a function of both overlap and separation distances between the two segments. Hence, we consider the evolution of β_0 with respect to the half lateral offset e (see Fig. 3), for two fixed separation distances $d/a = 0.1$ and $d/a = 0.3$. β_0 is computed for $0 \leq e/a \leq 3$, and plotted in Fig. 5 (left). The evolution of the corresponding length of the slipping zone on the lower fault (g/a) is shown in Fig. 5 (right). Overall, whether d/a equals 0.1 or 0.3, the system exhibits roughly the same dependence on e/a. For $e/a = 0$ (the faults completely overlap each other), slip cannot initiate simultaneously on both segments because of strong shadow effects, so that the stability limit is β_0^* and the length of the slipping zone on the shadowed segment is 0. As the length of overlap decreases (i.e. e/a increases), a collective instability occurs: the stability limit decreases and the slipping zone grows, rapidly for $d/a = 0.1$, slightly slower for $d/a = 0.3$. The minimum value of the lateral offset for which the shadow effect vanishes (no more locked zone, $g/a = 1$) is found for e/a ranging between 0.6 and 0.7 for both values of d/a. It is interesting to note that β_0 reaches a minimum, then increases and finally tends to β_0^* (the faults are independent). This minimum value of β_0 indicates a configuration of greatest instability, but the meaning of this has to be balanced by the limited amplitude of the variations of β_0.

6 CLASSIFICATION OF TWO-FAULTS SYSTEMS

Fault systems made of two parallel, similar, non-coplanar segments can be classified according to their global behaviour, which appears to depend on the system geometry. Three classes can be defined that only depend on the ratios d/a and e/a. In class I where the two segments do not or hardly overlap, instabilities develop all along both segments. Each segment tip, therefore, shows a stress singularity, so that four stress concentrations are observed in the medium (Fig. 6, left) ($d/a = 0.2$ and $e/a = 0.8$). In class II where segments significantly overlap, one of the segments is partly inhibited by the other. Hence, as one can see in Fig. 6 (right) ($d/a = 0.2$ and $e/a = 0.5$), only three stress singularities are observed, at both tips of the upper fault and at the outer tip only of the lower segment. Class III contains the configurations for which shadowing is complete, that is, one segment is totally inhibited by the other and unable to slip. It, therefore, shows no stress concentration at any of its tips. This occurs when the two segments completely overlap ($e = 0$). As considering this case further would not be very different from considering an isolated fault, class III will be left aside in the following. Classes I and II are plotted with respect to d/a and e/a on Fig. 7.

We now discuss the slip and stress profiles associated with the different classes, by examining the particular points A, B, C, D of

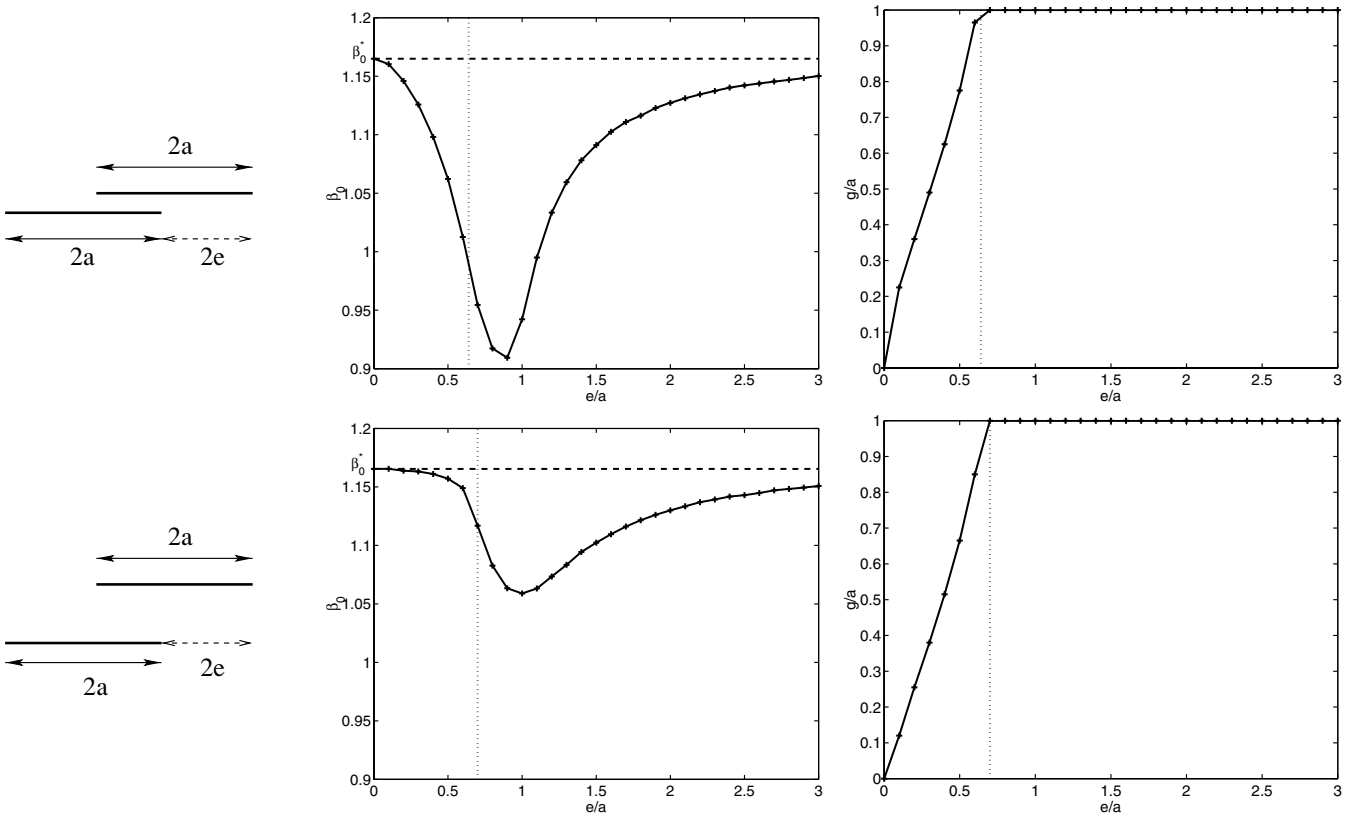

Figure 5. The stability limit β_0 (**left**) and slipping zone g/a (**right**) as functions of the ratio e/a, for $d/a = 0.1$ (**top**) and $d/a = 0.3$ (**bottom**).

the class diagram of Fig. 7. These points correspond to a constant separation distance $d/a = 0.1$ between the two segments, but to different values of their overlap (i.e. different e/a). Our computations show three different types of slip distributions on the faults, depending on the shape (and value) of the stress distribution in the vicinity of their tips (Fig. 8). For an isolated fault, the stress singularity at the fault tip can be approached by $\mathcal{K}/\sqrt{2\pi x}$ (e.g. Pucik 1972; Ishida 1973), where $\mathcal{K}$ is the stress intensity factor and x is the distance to the fault tip (the fault is supposed to lie on line $y = 0$). $\mathcal{K}$ can be numerically computed as $\lim_{x\to 0^+} \sqrt{2\pi x}\,\tau(x, 0)$. We use this formulation to determine the stress singularities at the tips of the faults we investigate below.

The first type of slip distribution is found on weakly interacting segments (point A, class I). In this case, each segment is slipping as a whole and shows an 'ellipsoidal' slip profile. All fault tips also have a significant stress singularity (Fig. 8a). The stress intensity factor $\mathcal{K}$ of each singularity defines the medium's resistance to fracture at the corresponding fault tip, hence the minimum strength that an hypothetical rigid barrier taken to lie at this tip would have to arrest the lateral propagation of the fault. In this first case of weakly interacting faults, the computation of all stress intensity factors shows that all stress singularities have the same strength. Hence, in systems of class I where rigid barriers would be replaced by breakable ones, active segments would tend to propagate in both directions alike.

Another type of slip distribution is found for systems belonging to class I but very close to the limit with class II, as is the case of point B (Fig. 7). On both segments, the ellipsoidal slip distribution appears 'stretched', in a symmetrical way, so that the maximum slip is shifted outward from the zone where faults interact. The resulting slip distribution is still elliptical near the outer fault tips, but is roughly linear near the inner fault tips (see Fig. 8b). The singularities at fault tips are all of the same order, but the stress intensity factors are higher at the outer fault tips, with ratios of about 100 between their maximum and minimum values (Fig. 8b). This may explain why the slip profiles are 'stretched' toward the outer fault tips. Also, if hypothetical rigid barriers at fault tips would be replaced by breakable ones, the outer barriers would be more damaged than the inner ones. If the medium has a homogeneous resistance to fracture, both segments will, therefore, preferentially propagate toward the exterior of the system.

As one leaves class I to enter class II, the shape of the slip profiles changes abruptly. A special case of this transition can be seen on Fig. 5. The length of the slipping zone is seen to rapidly decrease as the lateral offset decreases for a constant separation, that is, as the shadowing effect grows stronger. Faults in class II have asymmetric slip profiles: one segment has an undistorted 'ellipsoidal' slip distribution (as on Fig. 8a), while the slip profile of the other segment exhibits a quasi-linear long section in the inner part of the segment (as on Fig. 8b). Along this linear section, the slip decreases from its maximum to zero. No stress singularity is observed at this linear tip, which appears connected to a locked zone (Figs 8c and d). Indeed, the occurrence of stable slip on the upper fault prevents friction to exceed the static level on a significant part of the lower fault. This slip shadowing occurs regardless of the fact that the medium is everywhere homogeneous along both faults. In this case, the model predicts that the fault tip without stress singularity will not be able to propagate quasi-statically, whether there is a barrier or not.

Let us briefly summarize the meaning of the existence of nonlinearity and the multiplicity of eigenvalues. In the above case of two identical faults, we can find one or two eigenfunctions φ_0 for one

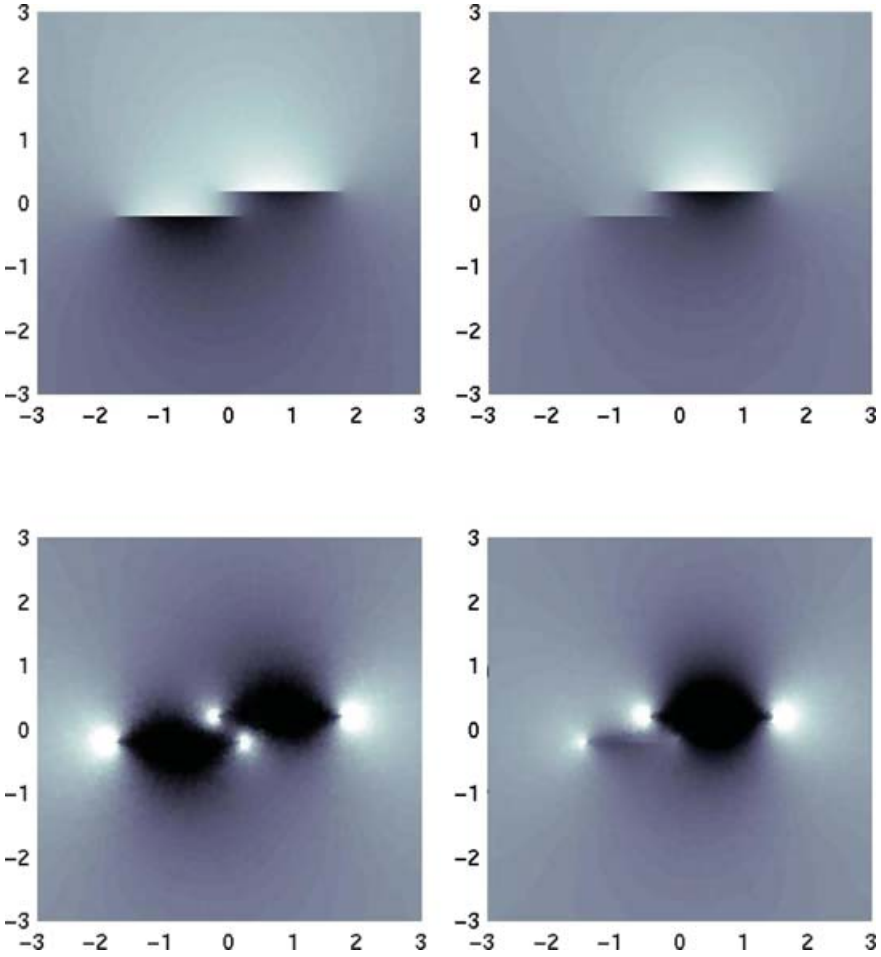

Figure 6. Displacement (**top**) and stress (**bottom**) fields, obtained by the computation of the non-linear static eigenfunction (β_0, φ_0). At left (class I, $d/a = 0.2$, $e/a = 0.8$), faults are mainly submitted to coplanar interaction and all fault tips have a stress singularity. At right (class II, $d/a = 0.2$, $e/a = 0.5$), non-coplanar interaction shadows the lower fault, creating a locked zone. As a consequence, the right tip of the lower fault has no stress singularity.

eigenvalue β_0. When there is only one eigenfunction, it is necessarily geometrically symmetrical with respect to the centre of the fault network (see for example Figs 8a or 8b). The interpretation of the multiplicity of eigenvalues is different whether they are found by a linear or non-linear analysis. In the linear case, a linear combination of the corresponding eigenfunctions is also an eigenfunction. In this case, each eigenfunction corresponds to one sliding segment, with the others being (almost) unaffected and, therefore, remaining stuck. In the non-linear case, a linear combination of the eigenfunctions of same eigenvalue is no longer a solution of our problem, because the segments do interact and the corresponding slipping zones are distinct. For example, in the case of two identical overlapping parallel fault segments, there are two symmetrical eigenfunctions with the same eigenvalue and symmetrical slip profiles (see Fig. 2); both eigenfunctions are equivalent.

The above classification concerns the static problem (11a)–(11d), that is, $\lambda^2 = 0$, but the same study can be performed for the dynamic one (10a)–(10d). We found that there is no abrupt transition between the quasi-static slip patterns and the ones corresponding to the dynamic onset of unstable slip. The slip distributions are quite similar in both cases, except that the strength of the interaction depends on β. More precisely, as λ_0^2 grows, the length of the locked zone increases, and the maximum slip on the dominant fault grows as well. Thus, the strength of the instability tends to confine the slip during the initiation phase. This feature is illustrated by Fig. 9. Note that this remark is not relevant to the long-term evolution of the system, since for $\lambda_0^2 > 0$ the weakening behaviour will be followed by a phase of rupture propagation, that is, the occurrence of a seismic event. The computation of the entire process, from the initiation phase to the end of the propagation of the seismic waves, leads to the slip profile plotted on Fig. 10 (here for $\alpha = 2.0$). Slip has occurred all along both segments, even in the zone that was locked during the initiation phase, but the slip has a linear shape in this region.

Note that our classification does not solely apply to fault systems made of two identical segments, since the slipping zones on both segments eventually reveal not to be of same length in class II. Hence our classification applies to any system made of two parallel, not fully overlapping segments. Class I corresponds to the configurations (symmetrical if the faults are of same length) in which the four fault tips are arrested by a barrier, whereas class II contains the configurations in which one fault tip is arrested by shadowing. The limit between these two classes is so narrow that it is very difficult to conclude, by considering only the geometry of a fault system, on the propagation of its faults and on the explanation (barrier or shadow) in case of arrest. However, we believe that, for a fault system having a geometry such that the system is close to the transition

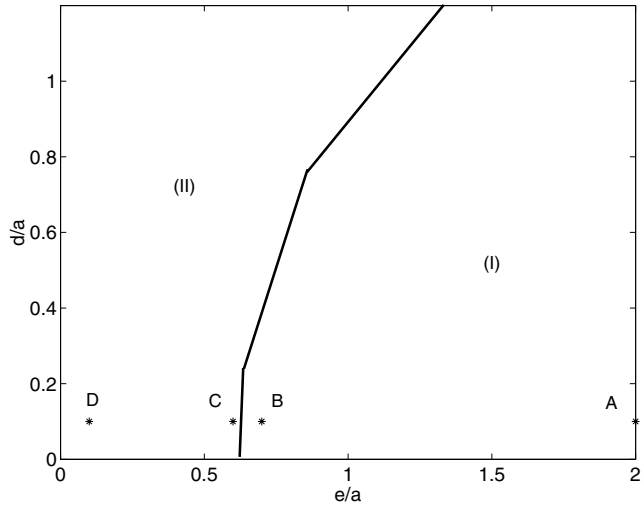

Figure 7. Diagram of fault systems classes. This diagram allows systems made of two segments to be classified as a function of their geometry (i.e. normalized separation and overlap distances). The criterion of classification is the number of stress singularities at the tips of the faults, obtained by the computation of the non-linear static eigenfunction (β_0, φ_0). In Class I, faults are loading each other and all fault tips show a stress singularity (total of 2 + 2 singularities). In Class II, fault interaction involves stress shadowing so that the shadowed fault tip has no singularity (total of 2 + 1 singularities). Points A, B, C and D refer to some particular computations that we have done and that are discussed in the text.

between classes I and II, it is reasonable to infer that one of its fault tips has stopped propagating because of shadow effects. This conclusion will be of considerable importance in the following.

7 APPLICATION TO A NON-PLANAR FAULT SYSTEM IN AFAR, AND IMPLICATIONS ON FAULT MECHANICS

Real faults grow as they accumulate slip during repeating earthquakes. Interseismic, more or less aseismic sliding may also occur and participate to their growth. The lack of observational data on repeating earthquakes on one given fault makes the mechanical processes of fault growth—that is, slip accumulation and lateral propagation - difficult to depict and characterize. We suggest that our modelling can build part of the bridge that necessarily extends between the only two data types that we have so far to work on, that is, instantaneous (seismic and dynamic) and cumulative (long-term and static) faulting. Faulting is the result of an effective weakening process that occurs as slip accumulates. The constitutive law on a cumulative, long-term fault can, therefore, be approximated by a simple slip-dependent friction law as the one taken in our modelling. Second, real faults have been shown to evolve at the limit of the stability (critical state, e.g. Sornette & Sornette 1989, and additional references in Scholz 2002). Together these suggest that the first non-linear static eigenmode of our model gives a reasonable first-order view of the state of real cumulative fault systems. Hence, a comparison can be drawn between the modelled slip profiles and those measured on real cumulative faults. Knowing the geometry of a fault system, the modelling allows dynamic stress interactions and weakening rates to be computed together on that system, until the solution approximating best the measured slip profiles is found. Although solutions are possibly non unique, 'too simple' (for the model does not include all the physical parameters that contribute to fault slip), and relying on *ad hoc* weakening functions, that kind of analysis allows highlighting robust general features in the fault system behaviour. We show it below.

As our model is built for antiplane slip, we compare our results to cumulative slip distributions measured on normal faults. Note that measured complete slip profiles are quite rare in the literature, particularly on large active faults capable of producing significant slip ruptures. The normal faults that dissect the Afar Depression (East Africa) are among the rare in the world to be at once active (i.e. generating earthquakes), large enough (L up to 100 km; vertical cumulative slip up to 1–2 km; maximum age ≈1–2 Ma) to have ruptured during a lot of repeating earthquakes and be capable of producing significant ones in the future, well studied (e.g. Tapponnier *et al.* 1990; Manighetti *et al.* 1998, 2001a,b; Hayward & Ebinger 1996), and having their cumulative slip profiles measured. We, therefore, chose to focus on some of these Afar faults. Manighetti *et al.* (2001a) already analysed the cumulative slip distributions on about 300 of these faults and systems. The major result of this analysis was to show that most cumulative slip profiles on the Afar faults show a self-similar envelop shape (hence, independent of scale, age, location, etc), being roughly triangular and asymmetric. The cumulative slip profiles thus have long, roughly linear sections, and some of them run along the entire fault length. These linear slip profiles were also shown to taper in the direction of overall (long-term) fault or system propagation. They were found on both interacting and isolated faults. These observations, together with some others elsewhere (see references in Manighetti *et al.* 2001a), resemble some of those we made on Fig. 8. This further suggests that a comparison between our modelled slip profiles and real ones can be drawn.

In the following, we focus on one of the non-coplanar Afar normal fault systems that has already been analysed by Manighetti *et al.* (2001a) (see that paper for a detailed description of faults and measurements). This fault system extends NW of the Asal rift, and offsets old lava piles (about 1 Ma). Note that it does not belong to any magmatic rift (as defined by Varet & Gasse 1978; Tapponnier *et al.* 1990; Manighetti *et al.* 1998, 2001b), so that its faults can be considered as representative of normal faults in 'common' amagmatic conditions. The system is made of three major fault segments (F1, F2, F3, see Fig. 11; fault segment tips are denoted T1–T6), *en echelon* arranged along a mean N125°E direction. Each segment is 20–30 km-long, while the overall system extends over about 70 km. Each segment is separated across-strike from the next by about 5–10 km ($2d$), and overlaps its immediate neighbor by about 7–10 km ($2a - 2e$). Their corresponding ratios d/a and e/a, therefore, are about 0.2–0.5 and 0.5–0.8, respectively. These make the two couples of segments F1–F2 and F2–F3 belonging to our class I, or to the transition zone between class I and class II. This remark is important because, in geological observations, faults are defined by their slipping zones, so that we are not 'allowed' to find large locked zones on the computed slip profiles. Finding each couple of segments outside class II gives us a chance to avoid such locked parts in the interacting triplet. In addition, as stated at the end of the previous subsection, finding a couple of faults close to the class transition gives precious information on the propagation of their inner tips.

The slip profiles measured on the three segments are shown in Fig. 12(b) (measurements are projected in the mean N125°E direction of the overall fault system). The maximum cumulative vertical offsets measured at the surface on F1, F2, and F3 are about 800, 1200 and 1000 m, respectively. On each segment, such huge slip has accumulated in the last million years (Manighetti *et al.* 2001a),

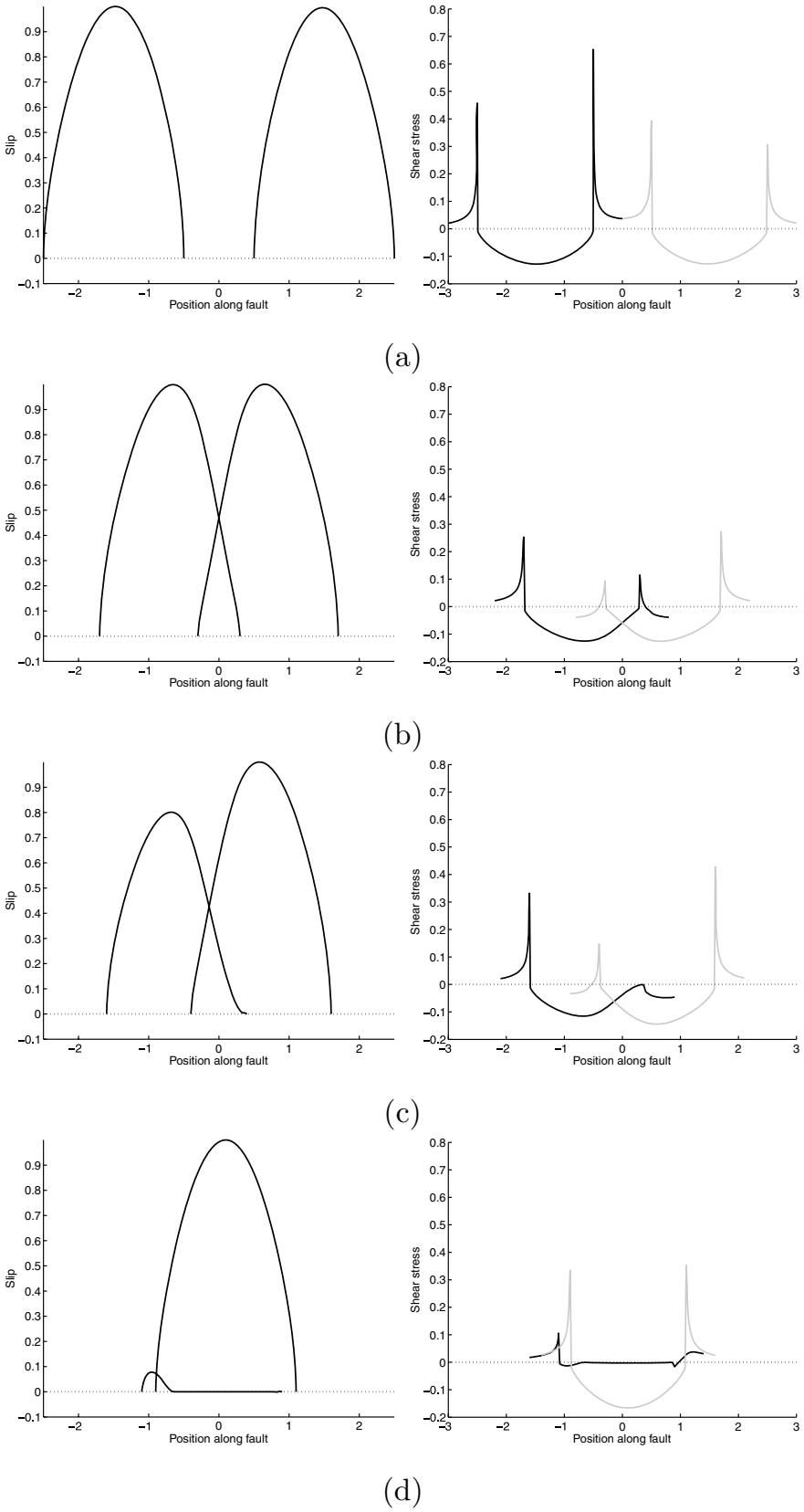

Figure 8. Slip and stress distributions deduced from the static eigenfunction for the different classes. Slip is at left; shear stresses on the faults are at right, only highlighted in black for the lower segment. Note that the relevant feature about the strength of the singularities is the stress intensity factor $\mathcal{K}$, whereas the value of the peak stress only depends on the discretization around the fault tip. (a) Point A: Two weakly interacting faults ($d/a = 0.1$ and $e/a = 1.5$) (b) Point B: Just before class transition I–II ($d/a = 0.1$ and $e/a = 0.7$) (c) Point C: Just after class transition I–II ($d/a = 0.1$ and $e/a = 0.6$) (d) Point D: Highly interacting faults ($d/a = 0.1$ and $e/a = 0.1$).

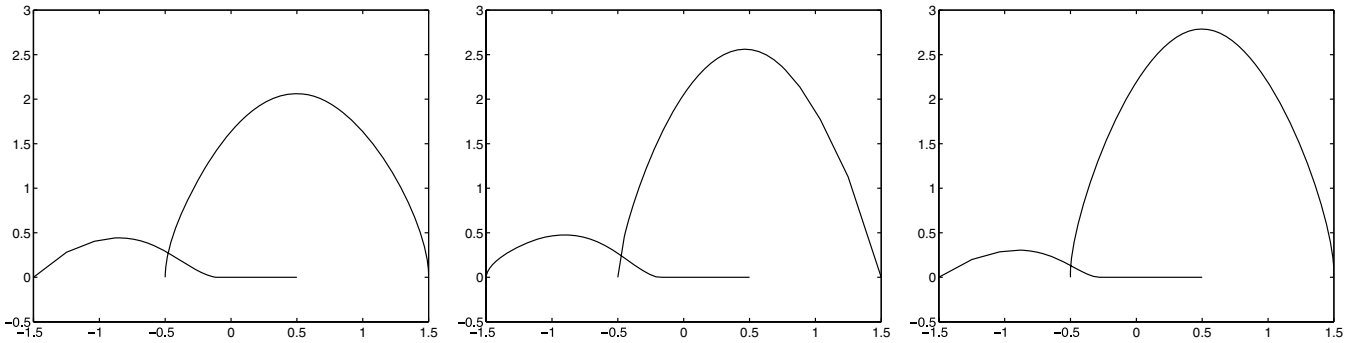

Figure 9. Slip profiles for increasing values of λ_0^2 (0.0, 0.5 and 1.0).

at a minimum vertical slip rate, therefore, averaging 1 mm yr^{-1}. The three profiles show different patterns. The slip distribution on F2 is rather symmetric and triangular, with high slip gradients on either side of the zone of maximum slip. The slip distribution on F3 is more asymmetric with the maximum slip being shifted toward the outer fault tip (T6), and slip decreasing roughly linearly from maximum to zero toward the other inner fault tip (T5). The slip distribution on F1 is even more asymmetric with the maximum slip being completely shifted at the inner fault tip (T2) and the rest of the slip decreasing linearly from its maximum to zero toward the other outer fault tip (T1). This latter slip profile has been shown by Manighetti *et al.* (2001a) to slant in the direction of F1 overall propagation. The high slip drop at the outer tip of F3 (T6) coincides with the NW termination of the volcano-tectonic, active Asal rift, which is therefore interpreted to act as a barrier to faulting lateral propagation (Manighetti *et al.* 2001a).

We use the average surface trace of the segments (Fig. 11) as our geometrical support Γ_f for the calculation of slip. We seek, through a trial-and-error approach, for the weakening rates $\eta(x, y)$ on the three fault segments that best allow the modelling (computation of the first static eigenfunction $(\beta_0, \varphi_0(x, y))$ to reproduce the observed slip profiles. As said above, we must find solutions lying either in class I or at the narrow limit between classes I and II.

Although we did not perform a strict inversion procedure, we found that the slip profile shapes that we produced were very sensitive both to the distribution of the weakening rate along the fault, and to the fault geometry Γ_f. The latter is known and fixed in our case.

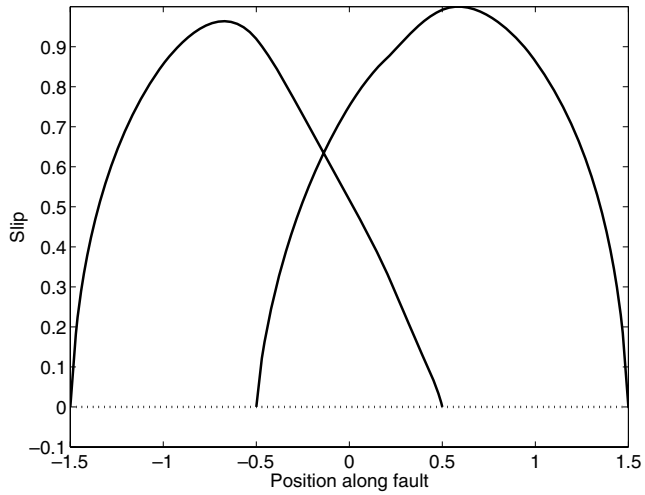

Figure 10. Slip profiles resulting from an entire seismic event for $\alpha = 2.0$.

Yet, our capability of finding a solution entirely in class I revealed to strongly depend on the position that we assigned to fault tips, especially tip T4. More generally, the geometry of the system—that favours strong interactions—made it quite difficult to avoid producing locked zones. As a matter of fact, although our final solution places both pairs of interacting segments in class I, they remain very close to class transition I–II.

To find the most appropriate weakening functions, we started by testing simple hypotheses such as constant or linearly varying weakening along the faults. Yet, those rapidly revealed not to be successful. In particular, considering a homogeneous weakening rate $(\eta(x, y) = 1)$, led to the development of large locked zones along the segments (class II) that are not observed in the data. The final, 'best-fitting' weakening profiles that we found $(\alpha(x, y) = \beta_0\, \eta(x, y))$, are presented in Fig. 12(a), together with the corresponding observed and modelled slip profiles (Fig. 12b) and the shear stress drops on the faults (Fig. 12c). While the three distributions of weakening differ in detail, they share a common characteristic: the weakening rate varies along fault strike, and decreases toward $x < 0$, hence in the NW direction shown to be that of overall fault propagation (see Fig. 12a). Beyond that common general trend, the weakening distributions show differences from one fault to the other. On fault F3, a simple, linear, NW decrease of the weakening rate allowed reproducing the slip profile quite well. By contrast, on F2, we had to add a bump in the middle of the weakening profile to succeed concentrating slip at the fault centre (Fig. 12a). On fault F1, a linear northwestward decrease of the weakening rate was not sufficient to reproduce the linear section of the measured slip profile, what forced us to consider instead a cubic decrease (Fig. 12a). We are aware that these *ad hoc* variations of the weakening rate may not be realistic. Yet, that the real slip profiles could not be reproduced without introducing such local variations confirms that the weakening rate varies along fault strike, and may increase with fault slip. All in all, the modelled slip profiles produced for F2 and F3 are quite similar to the observed profiles, hence are reasonable solutions. By contrast, the solution obtained for F1 is a bit weaker, as we do not reproduce the exact slip profile pattern. Such discrepancy on the most propagating segment of the system suggests that other factors than stress interaction and weakening process contribute as well to fault growth.

Note that, if stress shadowing had not been included in our calculations, the weakening functions above would not have succeeded alone in reproducing the observed slip profiles; a very small change in the shape of the weakening can produce an abrupt change in the slip of interacting faults (such as the disappearance of a significant portion of slipping zone), whereas it has only a weak influence on an isolated fault. Conversely, a linear slip function is produced along most of F1, in the absence of any particular interaction at T1. This

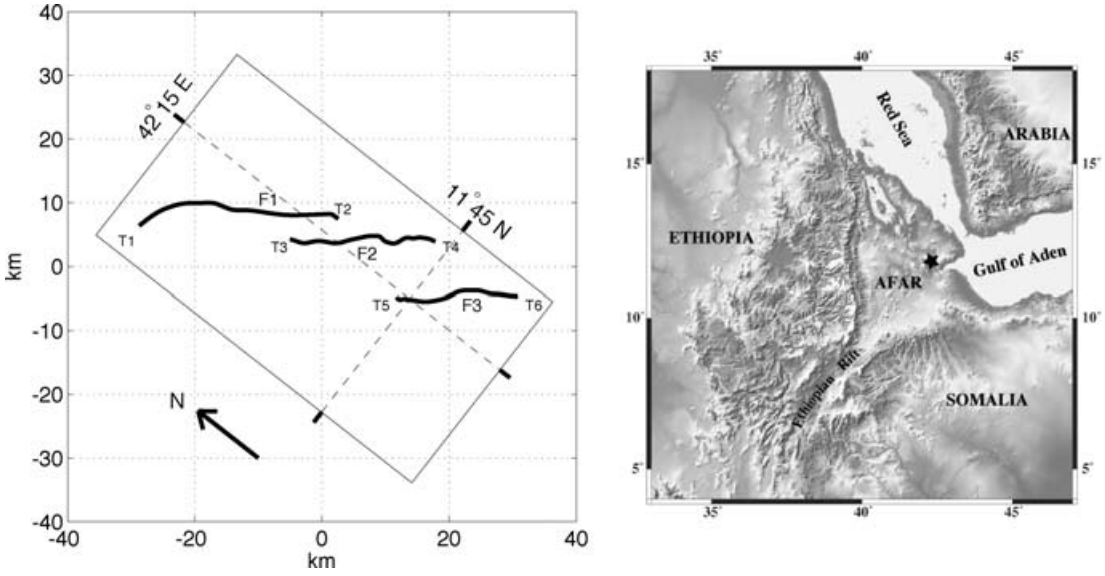

Figure 11. Fault system in Afar made of three *en echelon* normal fault segments. Inset shows general setting of Afar, and star locates the analysed fault system. Fault segments are denoted F1, F2 and F3 and fault tips T1,T2, . . . ,T6. This fault system geometry defines our geometrical support $\Gamma_f = F1 \cup F2 \cup F3$ for the slip.

further suggests that other factors than stress interaction and weakening contribute to fault slip profile shaping, particularly where the slip profiles exhibit long linear sections. Manighetti *et al*. (2004) have proposed that distributed off-fault inelastic strain may be one of such additional factors.

Having determined the optimal weakening rate distributions along the three F1–F2–F3 faults, we can analyse the stress distributions on and around the modelled faults. Note however that this state of stress does not include the 'pre-stresses', which are unknown. Computed shear stresses on the fault planes are shown in Fig. 12(c), while 2-D displacement and stress fields are represented in Fig. 13.

Although the faults are non planar, the state of stress at the fault tips can be observed on σ_{zn} (Fig. 12c). Tip T4 is observed to have the strongest stress intensity, while tip T2 has the weakest. This is because slip on F2 has put T2 in a stress shadow zone. Also, T2, together with T5, are close to the class transition I–II.

Fig. 14 shows together, at each mesh vertex, the calculated orientation of the plane submitted to maximal shear and the corresponding shear magnitude. Strictly speaking, Fig. 14 cannot be used to infer the location and orientation of the secondary faults likely to develop in the network, as Fig. 14 has been computed without including any pre-stress (i.e. regional state of stress). Both regional and local influences must be considered to infer secondary faulting. We limit our discussion to the effect of the change of stress associated with the stable sliding produced by our model. In coplanar fault systems, maximum shear is expected to apply on planes radially distributed at fault tips. This is the case at tip T6 where the largest stresses are observed. This suggests that T6 is presently arrested by a feature capable of impeding the lateral propagation of faulting. This feature could be the active volcano-tectonic Asal rift as suggested before. All other fault tips show different shear patterns. Stress orientations at tip T2 are strongly anisotropic, with a weak stress concentration in the orientation of the fault. This suggests that tip T2 is about to stop or to propagate in a new direction. In the region of

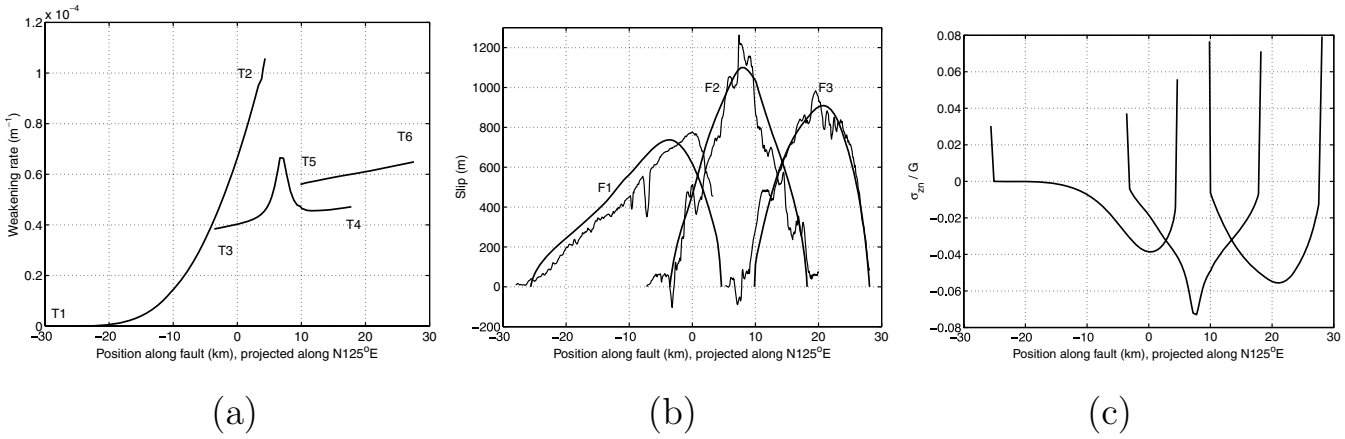

Figure 12. Results of the trial-and-error search for the three-faults system in Afar. From left to right, respectively: the deduced profiles of weakening along the faults, the computed slip profiles (thick lines) compared to the observed ones (thin lines), and the computed shear stress profiles on the faults.

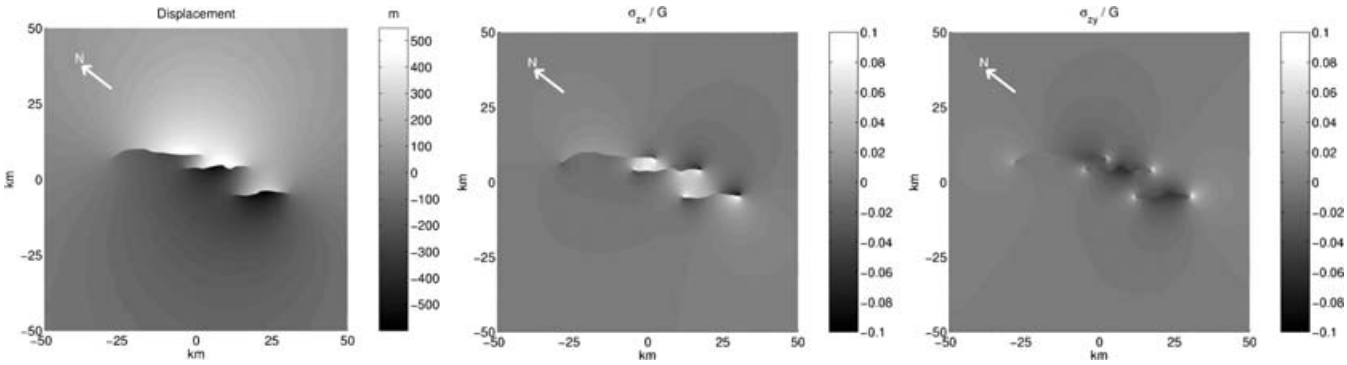

Figure 13. Displacement field, stress fields σ_{zx} and σ_{zy}.

interaction of F1 and F2, associated to tips T2 and T3, the direction of maximal shear is roughly perpendicular to both fault strikes while the shear magnitude is strong. A branching process may thus be expected (note that a starting connection is observed on the field). The situation is similar between F2 and F3 but shear stresses are weaker. As our model does not precisely reproduce the slip profile on F1, we cannot conclude on this fault's tips. We however believe that T1 has not yet encountered any barrier and is still propagating northwestward. Note that our model predicts a low weakening near T1, so that F1 would be growing without producing a large stress drop.

8 SUMMARY AND DISCUSSION

The aim of this paper was to understand how the fault geometry and the slip-weakening process combine within a non-coplanar, normal fault network to allow a slip instability to develop. This led us to analyse how stress interactions occur as the system starts slipping. The main result of our work is to show that, in non-coplanar normal fault systems, hence in most normal fault systems worldwide, the distribution and partition of the slip can be understood and predicted by using a modal approach of a meta-stable equilibrium that basically only includes a slip-weakening process. The geometry of the fault system also is, of course, an important parameter. Yet, many geological studies have shown that fault systems exhibit only a few self-similar geometries (e.g. Tchalenko 1970; Aydin & Schultz 1990), so that the arrangement of faults within a system is not random and can be precisely characterized and quantified at all scales. In particular, the non-coplanar fault geometry most commonly observed worldwide and at all scales, that is, the *en echelon* arrangement of faults, has been shown to satisfy precise scaling-laws, the major ones linearly relate the overlap distance to fault length (i.e. e/a = constant), and the separation distance to the overlap distance (i.e. d/a = constant) (e.g. Acocella *et al.* 2000, and references therein). Hence, the geometrical parameters can be reasonably determined and fixed in any problem of the type we address, so that the weakening rate distribution along the faults remains the major parameter that we must know to solve the problem.

In the first part of our work, we have formalized the problem and explored its non-linear modal solutions. The static formulation of the problem led to compute a stability criterion and the corresponding (meta-stable) static eigenfunction. We showed that the effect of non-coplanar interaction on fault stability is much more complex than the one of coplanar interaction. Indeed, even though faults within a system are all submitted to similar conditions, slip will not occur homogeneously on them. This comes from the fact that, in non-coplanar configurations, a slip patch on a part of the system may, depending on the system geometry and on its 'weakening configuration', enhance or impede slip on other sections of the system.

In the second part of our work, we have used our modelling to try reproducing the cumulative slip profiles measured on three real normal faults forming a large-scale *en echelon* system, and simultaneously determine the most appropriate weakening rate functions along the faults. For that, we assumed that cumulative slip profiles can be compared to the first static modal solution of the model (β_0,φ_0). An underlying question was to test whether stress interaction and weakening are the two major factors contributing to slip distribution within the fault system. This approach led to several results.

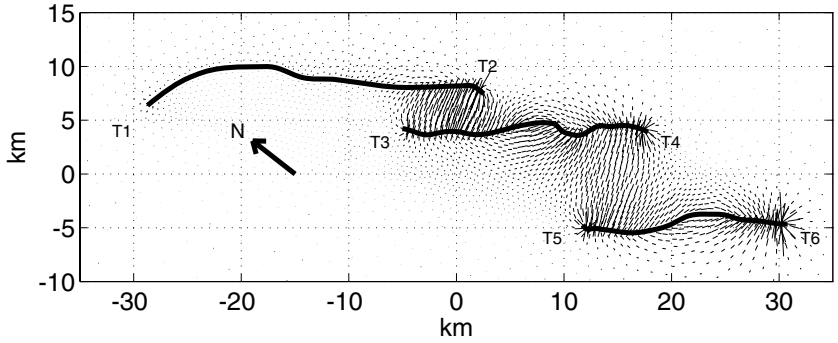

Figure 14. Orientation of the most solicited plane and unsigned magnitude of shear. At each point, the bar gives the orientation of the plane on which the shear stress is maximal, regardless of its sign. The length of the bar is proportional to the shear magnitude.

First, we were able to roughly reproduce the observed slip profiles. This is important because the slip profiles observed in Afar (Manighetti *et al.* 2001a) reveal to have an overall shape very different from that predicted by simple models of faults or cracks in a linear elastic medium. Such models predict that slip distributions should be elliptical or bell shaped. Instead, most Afar slip profiles are triangular, asymmetric, with long roughly linear sections slanting in direction of overall fault propagation. Note that similar quasi-linear slip profiles have been observed elsewhere in the world on both dip-slip (see references in Manighetti *et al.* (2001a)) and strike-slip faults, and for both cumulative and seismic deformation (Manighetti *et al.* 2005). Our modelling produces similar linear slip profiles, both in the static ($\lambda^2 = 0$) and dynamic cases.

So far, one common explanation to the observed linear slip profiles has been that friction on faults reduces with increasing slip (e.g. Bürgmann *et al.* 1994). Although this general statement must be true at a certain scale, our results show that it does not alone explain observations. Indeed, although a linear along-strike variation of slip weakening succeeds in explaining the slip distribution on fault F3 (Fig. 12a), linear-weakening profiles fail in explaining the other two slip profiles. In particular, we are forced to consider a cubic weakening decrease along F1, which exhibits the longest, most linear slip profile. Such a rapid weakening decrease, which leads to a very low weakening on a long section of the fault (10 km), seems quite unlikely. This may suggest that other factors not considered in our analysis may contribute to slip profile shaping on isolated, propagating faults.

Another common explanation to the observed linear slip profiles relies on fault interaction (Bürgmann *et al.* 1994; Martel 1997, 1999; Scholz 2002). Our modelling clearly demonstrates that, indeed, fault interaction can account for the development of steep linear slants inside shadow zones between interacting segments. Note however that long linear sections also develop in slip profiles in the absence of any interaction, as observed along fault F1.

Non-uniform boundary stresses were also advocated to account for the observed Afar linear slip profiles (e.g. Bürgmann *et al.* 1994). Our results demonstrate that this condition is not required, as the boundary conditions in our modelling are homogeneous, and yet linear slip profiles are produced.

The Afar linear slip profiles were also shown to taper in the direction of overall fault propagation (Manighetti *et al.* 2001a). Although our modelling cannot handle the process of fault propagation, we show that slip-weakening rate distributions on the analysed faults must, to be appropriate, decrease in the supposed direction of fault propagation. This gives supports to the propagation statement above.

Finally, our modelling also reproduces the high slip gradients observed at some fault tips. Such high slip drops, capable of dropping the slip from almost 1000 m high to 0 m in a distance of less than 10 km, were attributed to the existence of mechanical barriers. Our modelling also suggests the existence of such an obstacle to propagation at the eastern tip of F3 where the overall fault system ends abruptly.

We end by noting that our calculations, that assume a perfect linear elastic medium, lead to values for σ_{zn} that can reach 8 per cent of the shear modulus G (Fig. 12). This value is much higher than the value of the normal compression expected at 10 km depth in the crust, which is about 0.1 per cent of the classical instantaneous shear modulus G deduced from wave propagation speed. Of course, the tectonics reloads the fault, which compensates the stress drop due to such large slip. However, if the surrounding crust is purely elastic with the instantaneous value of G, it will be unreasonably overloaded. If elastic crustal behaviour is assumed, this suggests that the shear modulus appropriate for the Afar faults analysed at this long timescale should be smaller than the instantaneous value by one or two orders of magnitude. This supports the assumption that 'crustal damage' occurs in the medium surrounding the faults, resulting in a lowered effective shear modulus. Such off-fault damage could contribute to produce the linear slip profiles on isolated faults, as recently suggested by Manighetti *et al.* (2004).

ACKNOWLEDGMENTS

We are grateful to the anonymous reviewers and the Managing Editor C. Ebinger for their helpful comments. This work was supported by the French Ministry of Research through the ACI 'Prevention des Catastophes Naturelles', and by the INSU (CNRS) through the programme 'Dynamique et Evolution de la Terre Interne.'

REFERENCES

Acocella, V., Gudmundsson, A. & Funiciello, R., 2000. Interaction and linkage of extension fractures and normal faults: examples from the rift zone of Iceland, *J. Struct. Geol.,* **22,** 1233–1246.

Aochi, H. & Madariaga, R., 2003. The 1999 Izmit, Turkey, earthquake: nonplanar fault structure, dynamic rupture process and strong ground motion, *Bull. seism. Soc. Am.,* **93**(3), 1249–1266.

Aydin, A. & Schultz, R.A., 1990. Effect of mechanical interaction on the development of strike-slip faults with echelon patterns, *J. Struct. Geol.,* **12,** 123–129.

Badea, L., Ionescu, I. & Wolf, S., 2004. Domain decomposition method for dynamic faulting under slip-dependent friction, *J. Comp. Phys.,* **201,** 487–510.

Baud, P. & Reuschlé, T., 1997. A theoretical approach to the propagation of interacting cracks, *Geophys. J. Int.,* **130,** 460–468.

Beer, G. & Meek, J.L., 1981. 'Infinite domain' elements, *Int. J. num. Meth. Engng.,* **17,** 43–52.

Bürgmann, R., Pollard, D.D. & Martel, S.J., 1994. Slip distribution on faults: effects of stress gradients, inelastic deformation, heterogeneous host-rock stiffness, and fault interaction, *J. Struct. Geol.,* **16,** 1675–1690.

Campillo, M., Favreau, P., Ionescu, I.R. & Voisin, C., 2001. On the effective friction law of an heterogeneous fault, *J. geophys. Res.,* **106,** 16 307–16 322.

Campillo, M., Dascalu, C. & Ionescu, I.R., 2004. Instability of a periodic system of faults, *Geophys. J. Int.,* **159,** 212–222.

Comninou, M.A. & Dunders, J., 1975. The angular dislocation in a half-space, *J. Elasticity,* **5,** 203–216.

Crider, G.C. & Pollard, D.D., 1998. Fault linkage: three-dimensional mechanical interaction between echelon normal faults, *J. geophys. Res.,* **103,** 24 373–24 391.

Dascalu, C., Ionescu, I.R. & Campillo, C., 2000. Fault finiteness and initiation of dynamic shear instability, *Earth planet. Sci. Lett.,* **177,** 163–176.

Fitzenz, D. & Miller, S.A., 2001. A forward model for earthquake generation on interacting faults including tectonics, fluids, and stress transfer, *J. geophys. Res.,* **106**(B11), 26 689–26 706.

Harris, R.A. & Day, S.M., 1993. Dynamics of fault interaction: parallel strikeslip faults, *J. geophys. Res.,* **98,** 4461–4472.

Hayward, N.J. & Ebinger, C.J., 1996. Variations in the along-axis segmentation of the Afar Rift system, *Tectonics,* **15**(2), 244–257.

Ionescu, I. & Wolf, S., 2005. Interaction of faults under slip-dependent friction. Non-linear eigenvalue analysis., *Math. Meth. Appl. Sci.,* **28,** 77–100.

Ishida, M., 1973. Method of Laurent series expansion for internal crack problems, in *Mechanics of Fracture 1: Methods of Analysis and Solutions of Cracks Problems*, ed. Sih, G.C., (Sithoff and Noordhoff Ed., Leyden, The Netherlands).

King, G.C.P., Stein, R.S. & Lin, J., 1994. Static stress changes and the triggering of earthquakes, *Bull. seism. Soc. Am.,* **84,** 935–953.

Manighetti, I., Tapponnier, P., Gillot, P.-Y., Courtillot, V., Jacques, E., Ruegg, J.-C. & King, G., 1998. Propagtion of rifting along the Arabia-Somalia plate boundary: into Afar, *J. geophys. Res.,* **103,** 4947–4974.

Manighetti, I., King, G.C.P., Gaudemer, Y., Scholz, C.H. & Doubre, C., 2001a. Slip accumulation and lateral propagation of active normal faults in Afar, *J. geophys. Res.,* **106,** 13 667–13 696.

Manighetti, Tapponnier, P., Courtillot, V., Gallet, Y., Jacques, E., & Gillot P.-Y., 2001b. Strain transfer between disconnected, propagating rifts in Afar, *J. geophys. Res.,* **106,** 13 613–13 665.

Manighetti, I., King, G. & Sammis, C.G., 2004. The role of off-fault damage in the evolution of normal faults, *Earth planet. Sci. Lett.,* **217,** 399–408.

Manighetti, I., Campillo, M., Sammis, C.G., Mai, P.M. & King, G., 2005. Evidence for self-similar, triangular slip distributions on earthquakes; implications for earthquake and fault mechanics, *J. geophys. Res.,* **110,** B05302, doi:10.1029/2004JB003174.

Martel, S.J., 1997. Effects of cohesive zones on small faults and implications for secondary fracturing and fault trace geometry, *J. Struct. Geol.,* **19,** 835–847.

Martel, S.J., 1999. Mechanical controls on fault geometry, *J. Struct. Geol.,* **21,** 585–596.

Ohnaka, M. & Kuwahara, Y., 1990. Characteristic features of local breakdown near a crack-tip in the transition zone from nucleation to unstable rupture during stick-slip shear failure, *Tectonophysics,* **175,** 197–220.

Ohnaka, M., Kuwahara, Y. & Yamamoto, K., 1987. Constitutive relations between dynamic physical parameters near a tip of the propagating slip zone during stick slip shear failure, *Tectonophysics,* **144,** 109–125.

Okada, Y., 1992. Internal deformation due to shear and tensile faults in a half-space, *Bull. seism. Soc. Am.,* **82,** 1018–1042.

Pucik, T.A., 1972. Elastostatic interaction in an infinite plane, *PhD thesis*, Calif. Inst. of Technol., Pasadena, California.

Robinson, R. & Benites, R., 1995. Synthetic seismicity models of multiple interacting faults, *J. geophys. Res.,* **100,** 18 229–18 238.

Scholz, C.H., 2002. *The Mechanics of Earthquakes and Faulting*, 2nd edn, Cambridge University Press Ed., London.

Segall, P. & Pollard, D.D., 1980. Mechanics of discontinuous faults, *J. geophys. Res.,* **85,** 4337–4350.

Sornette, A. & Sornette, S., 1989. Self-organised criticality and earthquakes, *Europhys. Lett.,* **9,** 197–202.

Spyropoulos, C., Scholz, C. & Shaw, E., 2002. Transition regimes for growing crack populations, *Phys. Rev. E,* **65,** 056105.

Tapponnier, P., Armijo, R., Manighetti, I. & Courtillot, V., 1990. Bookshelf faulting and horizontal block rotations between overlapping rifts in southern Afar, *Geophys. Res. Lett.,* **17,** 1–4.

Tchalenko, J.S., 1970. Similarities between shear zones of different magnitudes, *Geol. soc. Am. Bull.,* **81,** 1625–1640.

Uenishi, K. & Rice, J.R., 2002. Universal nucleation length for slip-weakening rupture instability under non-uniform fault loading, *J. geophys. Res.,* **108**(B1), 10.1029/2001JB001681.

Umeda, Y., Yamashita, T., Tada, T. & Kame, N., 1996. Possible mechanism of dynamic nucleation and arresting of shallow earthquake faulting, *Tectonophysics,* **261,** 179–192.

Varet, J. & Gasse, F., 1978. Geology of central and southern Afar, report, Cent. Nat. de la Rech. Sci., Paris.

Voisin, C., Campillo, M., Ionescu, I.R., Hassani, R. & Nguyen, Q.L., 2002. Process and signature of initiation on a finite fault system: a spectral approach, *Geophys. J. Int.,* **148**(1), 120–131.

Willemse, J.M.E., 1997. Segmented normal faults: correspondence between three-dimensional mechanical models and field data, *J. geophys. Res.,* **102,** 675–692.

Zienkiewicz, O.C. & Zhu, J.Z., 1987. A simple error estimator and adaptive procedure for practical engineering analysis, *Int. J. Numer. Meth. Engrg.,* **24,** 337–357.